CHEMISTRY OF MATERIALS

pubs.acs.org/cm

Article

Engineering of a Coupled Nanocomposite as a High-Performance Protonic Ceramic Fuel Cell Cathode

Liang Han, Jiawei Zhang,* Minda Zou, Yuchen Zhang, Hongkui Zheng, Ryo Kitamura, Yanfei Cai, Talia Marie Sebastian, Ted Burye, Dong Ding, Zeyu Zhao, Kai He, and Jianhua Tong*

Cite This: *Chem. Mater.* 2024, 36, 11288−11295

Read Online

ACCESS | Metrics & More | Article Recommendations | Supporting Information

ABSTRACT: The lack of high-performance cathode catalysts is a salient issue that bedeviled the commercialization of protonic ceramic fuel cells (PCFCs). Here, we report a remarkable electrocatalytic activity and stability enhancement of cathode electrodes by engineering a coupled nanocomposite. The as-prepared $Pr_{0.3}(Ba_{0.5}Sr_{0.5})_{0.7}Co_{0.8}Fe_{0.2}O_{3-\delta}$ nanocomposite possesses a bulk cubic phase on which homogeneous and intimate orthorhombic $PrCo_{0.5}Fe_{0.5}O_{3-\delta}$ nanoparticles are uniformly decorated. X-ray diffraction and Raman spectroscopy reveal the excellent thermal stability of the nanocomposite. It achieves a high peak power density of 1.02 W cm^{-2} based on protonic electrolytes at 600 °C. No noticeable structural degradation is observed over ∼210 h at 550 °C according to scanning electron microscopy analysis. This work demonstrates an effective strategy to boost the performance of perovskite oxides for PCFCs via nanocomposite engineering. It may apply to other catalyst designs and discoveries, such as for batteries, electrolyzers, and membrane reactors.

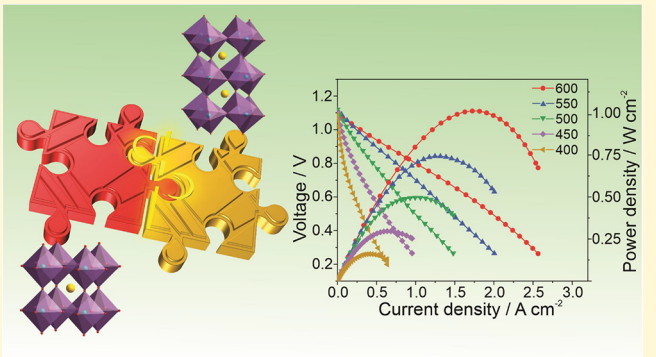

INTRODUCTION

Over the last few decades, protonic ceramic fuel cells (PCFCs) have garnered universal interest due to their impressive efficiency and exceptional sustainability. They directly convert various fuels, such as H_2, hydrocarbons, and ammonia, into electric power at intermediate temperatures ranging from 400 to 700 °C.[1,2] However, a significant issue that bedeviled their commercialization is the lack of high-performance cathode catalysts, as the reducing operating temperature considerably aggravates the kinetically sluggish oxygen reduction reaction (ORR).[3,4] One overarching approach to realizing the enormous benefits of PCFCs is the discovery and synthesis of active and stable cathode electrocatalysts.

Researchers have made significant efforts to synthesize advanced cathode electrocatalysts for PCFCs.[5,6] One promising candidate is composite cathodes, which offer a comprehensive performance by taking advantage of synergic effects.[3,7,8] For example, the conventional cathodes are obtained by mechanically mixing the mixed ionic−electronic conductors (MIECs) with the protonic conducting phase.[9] Alternatively, sophisticated deposition techniques, such as pulsed laser deposition, atomic layer deposition, and infiltration, are developed to fabricate complex nanoheterostructures with finely controlled size.[10,11] However, these routes experience at least one of the following challenges: inhomogeneous microcomposites with limited active contact areas, long charge transport paths, complicated and laborious experiment procedures, low area of quasi-two-dimensional components' boundaries, and limited loading mass. Worse still, the as-prepared composite cathodes are unstable because of their weak interaction with substrate components.[12] Very recently, some studies found that the decomposition of composite cathodes could lead to the formation of new crystal phases, which account for the improvement of the cathodic properties.[13,14] These studies spark interest in rationally synthesizing new composite cathodes to overcome existing drawbacks by leveraging the synergistic effects of different components.

Herein, we introduced a nanocomposite engineering strategy to boost the performance of the cathode electrode in PCFCs. $Ba_{0.5}Sr_{0.5}Co_{0.8}Fe_{0.2}O_{3-\delta}$ (BSCF) has been regarded as an excellent ORR electrocatalyst due to its superior MIEC properties.[15] More importantly, several studies have demonstrated that BSCF possesses protonic conductivity, which makes it a potential cathode material for PCFCs.[15−18] Nevertheless, its structural instability at intermediate temperatures impedes its application as a cathode in PCFCs.[15,19]

Received: August 25, 2024
Revised: October 17, 2024
Accepted: October 21, 2024
Published: November 4, 2024

Downloaded via UNIV OF CALIFORNIA IRVINE on February 27, 2025 at 11:16:33 (UTC).
See https://pubs.acs.org/sharingguidelines for options on how to legitimately share published articles.

ACS Publications

© 2024 American Chemical Society

Starting from the precursor with a nominal composition of $Pr_{0.3}(Ba_{0.5}Sr_{0.5})_{0.7}Co_{0.8}Fe_{0.2}O_{3-\delta}$ ($Pr_{0.3}$BSCF), a twin phase nanocomposite is produced via the "self-assembly" process. The bulk cubic phase is decorated with homogeneous and intimate orthorhombic $PrCo_{0.5}Fe_{0.5}O_{3-\delta}$ nanoparticles. The nanocomposite shows excellent thermal stability in humid air and superior electrocatalytic performances. It achieves a peak power density (PPD) of 1.02 W cm^{-2} (2.27 times that of the BSCF cathode) based on $BaCe_{0.7}Zr_{0.1}Y_{0.1}Yb_{0.1}O_{3-\delta}$ (BCZYYb) electrolytes at 600 °C and exhibit excellent stability over 210 h with no noticeable degradation at 550 °C.

EXPERIMENTAL DETAILS

Chemicals. Barium carbonate ($BaCO_3$, 99.8%), barium nitrate ($Ba(NO_3)_2$, 99+%), strontium nitrate ($Sr(NO_3)_2$, 99+%), cobalt(II) nitrate hexahydrate ($Co(NO_3)_3{\cdot}6H_2O$, 98−102%), iron(III) nitrate nonahydrate ($Fe(NO_3)_3{\cdot}9H_2O$, 98+%), ethylenediaminetetraacetic acid (EDTA, 99.4%), cerium oxide (CeO_2, 99.9%), nickel(II) oxide (NiO, 99%), ytterbium(III) oxide (Yb_2O_3, 99.9%), yttrium(III) oxide (Y_2O_3, 99.9%), isopropanol (IPA, 70% v/v), and 1-butanol were purchased from Alfa Aesar. Praseodymium(III) nitrate hexahydrate ($Pr(NO_3)_3{\cdot}6H_2O$, 99.9+%) and zirconium(IV) oxide (ZrO_2, 99.7%) were purchased from Sigma-Aldrich. The alpha-terpineol (97+%) and citric acid monohydrate (99.5%) were purchased from ACROS Organics. The ammonium hydroxide ($NH_3{\cdot}H_2O$, 28−30% w/w) was purchased from LabChem. All chemicals were used as received without further purification.

Preparation of the Electrolyte. The BCZYYb electrolyte precursor powder was synthesized by a solid-state reaction method. Stoichiometric raw materials of $BaCO_3$, ZrO_2, CeO_2, Y_2O_3, and Yb_2O_3 were mixed by planetary ball milling at 300 rpm for 12 h in ethanol. The dried mixture was calcined at 1100 °C for 10 h in air. The above process was repeated once, and the final powder was ball milled at 400 rpm for 12 h followed by drying.

Preparation of the Cathode Precursor $Pr_{0.3}$BSCF Nanocomposite. The cathode precursor powder was synthesized using a modified Pechini method. First, stoichiometric amounts of $Pr(NO_3)_3{\cdot}6H_2O$, $Ba(NO_3)_2$, $Sr(NO_3)_2$, $Co(NO_3)_2{\cdot}6H_2O$, and $Fe(NO_3)_3{\cdot}9H_2O$ were dissolved in an appropriate amount of distilled water with continuous stirring. Then, the citric acid and EDTA were added to form a clear solution. The molar ratio of total metal ions/EDTA/citric acid was set as 1:1.5:1.5. The pH value of the solution was adjusted to around 9 by slowly adding a proper amount of $NH_3{\cdot}H_2O$ under continuous stirring. A viscous gel was obtained with continuous heating and stirring to evaporate the excess water. After that, the gel was carbonized in a box oven at 150 °C for 48 h. The carbonized powder was calcined at 600 °C for 5 h to remove most of the carbon. The powder was further ball-milled on a roller with YSZ balls in 1-butanol for 7 days and then dried at 150 °C followed by firing at 400 °C for 3 h to remove butanol thoroughly. Finally, the cathode precursor powder was ball-milled again in isopropyl alcohol and dried at 90 °C to obtain the final cathode precursor powder. The same procedure was used to prepare the BSCF precursor powder.

Preparation of Cathode Precursor Pastes. The mixture consisting of the precursor powder, dispersant (20 wt % Solsperse 28000 (Lubrizol Corp.) in terpineol solution), and binder (5 wt % V-600 (Heraeus company) in terpineol solution) in a weight ratio of 15:3:1 was mixed by manually grinding for 45 min in an agate mortar with an agate pestle.

Fabrication of Symmetrical Cells. The BCZYYb electrolyte pellets were fabricated using the solid-state reactive sintering method described below. The BCZYYb + 1 wt % NiO electrolyte precursor powders were pressed into green pellets under 350 MPa for 120 s in the circular carbon-aided steel die set. The green electrolyte pellets have a diameter of 19 mm and a thickness of ∼2 mm. After the mixture was sintered at 1450 °C for 18 h, the BCZYYb electrolyte pellets were obtained. After that, the cathode precursor paste was screen-printed on both sides of the polished electrolyte pellets and then annealed at 950 °C for 4 h. The silver mesh was attached to the electrode surfaces to work as a current collectors.

Fabrication of Single Cells. The as-prepared BCZYYb electrolyte powder in Section (Preparation of the Electrolyte) was mixed with or without 60 wt % NiO and dispersant, solvent, binder, and plasticizer to form the NiO/BCZYYb hydrogen electrode slurries and BCZYYb electrolyte. Then, these two green tapes were fabricated by the tape casting method and laminated with one electrolyte layer and three hydrogen electrode layers, as supported by hot pressing. The laminated tape was cut into cells of Φ11.1 mm (7/16 in.), after which its polymer composition was burnt by presintering at 920 °C. Subsequently, the presintered cells were sintered at 1430 °C for 5 h for the electrolyte densification to get the final half-cells. After that, the cathode precursor paste was screen-printed on the electrolyte's top and then annealed at 950 °C for 4 h. The silver mesh was attached to the electrode surfaces to work as current collectors.

Characterization. The phase structures were characterized with X-ray diffraction (XRD) patterns recorded by the Rigaku MiniFlex 600 with monochromatic Cu Kα radiation and a voltage of 40 kV. The angle range was 15−90°, and the scanning speed was 2° min^{-1}. The microstructures were characterized by a scanning electron microscope (SEM, Hitachi Regulus 8230, Hitachi, Ltd., Tokyo, Japan) operating at 15 kV. The nanocomposites' composition and crystal structure were characterized by a spherical aberration-corrected transmission electron microscope (JEOL JEM-ARM300F Grand ARM TEM). To make the energy-dispersive X-ray spectroscopy (EDS) data accurate, we used Pr (L-series), Fe (K-series), and Co (K-series) relative intensities of a standard sample with known stoichiometry ($PrBa_{0.5}Sr_{0.5}Fe_{0.5}Co_{1.5}O_{5+\delta}$) to calibrate the Pr, Fe, and Co compositions. The atomic model was built according to the standard Powder Diffraction File (PDF) information. The X-ray photoelectron spectroscopy (XPS) measurements were performed on a PHI VPIII instrument. The binding energies were calibrated to the adventitious C 1s peak at 284.8 eV. The oxygen temperature-programmed desorption (O_2-TPD) measurements were monitored by a mass spectrometer (Cirrus 2 (MKS)). Raman spectra were excited by a Kr^+ laser (Innova 100, Coherent) line at 476.2 nm, collected in a backscattering geometry, and analyzed by a spectrograph (Triplemate1377, Spex) equipped with a CCD camera (Andor, IDus). The power at the sample was between 10 and 30 mW, and the total spectrum collection time was 100 s.

Electrochemical Measurement. Symmetrical cells and single cells were measured with a PARSTAT MC-1000 multichannel potentiostat. The electrochemical impedance spectra (EIS) were conducted under the open circuit voltage conditions (OCVs) at a temperature range from 300 to 650 °C under wet flowing air (room temperature water bubbler, 50 mL min^{-1}) using a signal amplitude of 10 mV in the frequency range of 0.01 Hz −1 MHz. The results obtained from EIS were further analyzed by using the ZView software. The single-cell performance was tested with 50 mL min^{-1} H_2 as fuel and 150 mL min^{-1} air as oxidant. A long-term stability test was carried out under a constant current density of 300 and 500 mA cm^{-2} at 550 °C.

RESULTS AND DISCUSSION

In a typical synthesis of $Pr_{0.3}$BSCF, nitrate metal precursors were mixed with ethylenediaminetetracetic acid and citric acid and then went through the sol−gel process (see the Supporting Information for detailed synthesis). Figure 1a shows the XRD patterns of as-prepared $Pr_{0.3}$BSCF powders. Similar to the BSCF, the diffraction peaks of $Pr_{0.3}$BSCF can be indexed to the cubic *Pm*-3*m* phase and show no extra crystal phase. However, all their peaks shift to higher angles, indicating the lattice shrinkage due to the involvement of praseodymium (Pr) in the crystal lattice. It is caused by the fact that Pr^{3+} possesses a smaller ionic radius (1.29 Å) than Ba^{2+} (1.61 Å) and Sr^{2+} (1.44 Å). The XPS spectrum of Pr 3d further confirmed the successful doping of Pr into the crystal lattice of BSCF (Figure

https://doi.org/10.1021/acs.chemmater.4c02386
Chem. Mater. 2024, 36, 11288−11295

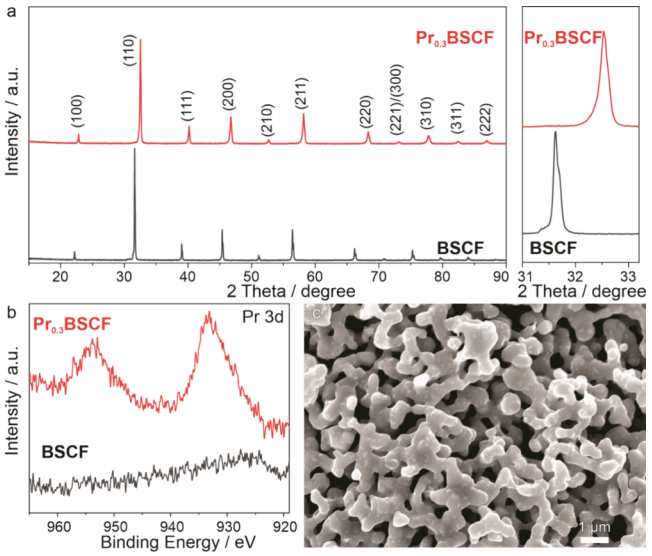

Figure 1. Crystal structure and microstructure characterizations of the $Pr_{0.3}BSCF$ nanocomposite. (a) XRD patterns, (b) XPS spectra of Pr 3d of as-synthesized $Pr_{0.3}BSCF$ nanocomposite and BSCF, and (c) SEM image of the $Pr_{0.3}BSCF$ nanocomposite.

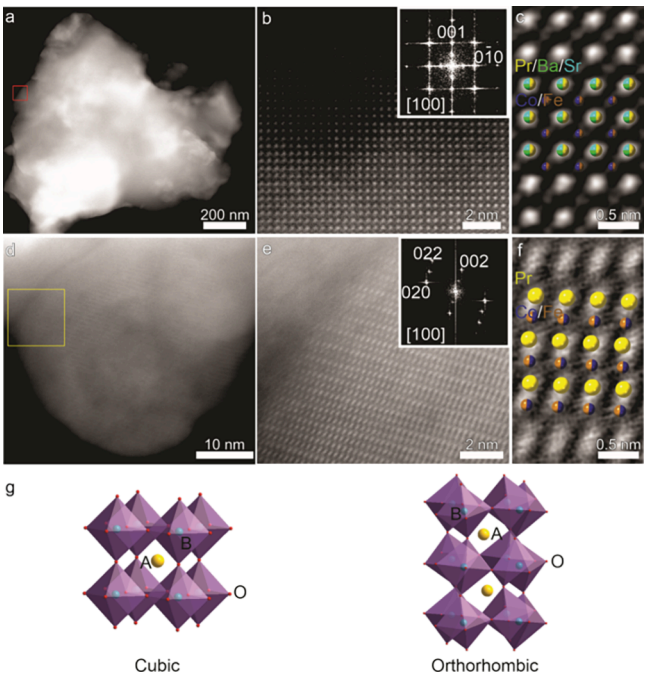

Figure 2. Crystal phase characterizations of the $Pr_{0.3}BSCF$ nanocomposite. (a) HAADF-STEM image of the bulk particle. (b) High-resolution HAADF-STEM image taken from the red-boxed region in panel a with an inset FFT pattern showing the cubic structure along the [100] zone axis. (c) FFT-filtered enlarged HAADF-STEM image with an overlaid atomic model of the cubic crystal lattice. (d) HAADF-STEM image of a secondary-phase nanoparticle. (e) High-resolution HAADF-STEM image taken from the yellow-boxed region in panel d with an inset FFT pattern showing the orthorhombic structure along the [100] zone axis. (f) The enlarged HAADF-STEM image with an overlaid atomic model of orthorhombic crystal lattice. (g) Schematics of the cubic and orthorhombic crystal structures.

1b). The EDS result showed that all the Pr is successfully doped into the BSCF (Figure S1). Surprisingly, different from the smooth surface of BSCF powders (Figure S2), the SEM analysis of $Pr_{0.3}BSCF$ powders shown in Figure 1c indicated uniform nanoparticles with a size of 50 nm decorated on the 500 nm bulk particles. The striking difference between the morphologies of $Pr_{0.3}BSCF$ and BSCF implies that the new crystal phase may form.

We used a spherical aberration-corrected scanning transmission electron microscope (STEM) to study the crystal structure and composition of the $Pr_{0.3}BSCF$ nanocomposite. Figure 2a shows the high-angle annular dark-field STEM (HAADF-STEM) image of a bulk particle. The high-resolution HAADF-STEM and the corresponding fast Fourier transform (FFT) images reveal that the bulk particle has a cubic unit cell with the *Pm*-3*m* space group, consistent with the above XRD result (Figure 2b,c). The cubic atomic model matched perfectly with the crystal lattice of the bulk particle, further demonstrating its cubic crystal structure. Meanwhile, EDS mapping suggests a homogeneous distribution of Pr, Ba, Sr, Co, Fe, and O (Figure S3, Table S1). When we looked at the decorated small secondary nanoparticle, we found that it displays a crystal structure distinct from that of the bulk particle (Figure 2d–f). Its FFT image corresponds to the orthorhombic structure along the [100] zone axis. As shown in Figure 2e, the orthorhombic atomic model with the *Pbnm* space group can perfectly overlap the crystal lattice of the small secondary nanoparticle. Unexpectedly, the EDS data obtained at the small secondary nanoparticle confirm that it comprises $PrCo_{0.5}Fe_{0.5}O_{3-\delta}$ (Figures S4 and S5). Considering the overall analyses, we concluded that the as-prepared $Pr_{0.3}BSCF$ nanocomposite comprised two crystal structures. The secondary orthorhombic nanoparticles were uniformly distributed across the bulk cubic phase. In contrast with the cubic phase, the orthorhombic structure has lower symmetry arrangements, which are caused by the tilting of the BO_6 octahedra.[18,19] This distorted structure is represented in Figure 2g. The smaller Pr^{3+} cations' displacement of the larger A-site Ba and Sr cations of BSCF causes the cubic structure to be locally distorted into the orthorhombic structure, which possesses unequal B–O bond lengths.[20,21]

XPS spectra systematically investigated the influence of Pr-doping on the electronic structure change of BSCF. Figure 3a presents the XPS spectra for O 1s of $Pr_{0.3}BSCF$ and BSCF. The peaks can be deconvoluted into four characteristic peaks corresponding to lattice oxygen species (O^{2-}, 528.6 eV), surface adsorbed oxygen species (O_2^{2-}/O^- for 529.9 eV, $-OH/O_2$ for 531.2 eV), and adsorbed molecular water (H_2O, 532.4 eV).[22,23] For the lattice oxygen species, the binding energy for the $Pr_{0.3}BSCF$ nanocomposite (528.6 eV) is slightly higher than that for BSCF (528.5 eV), suggesting a weaker interaction between lattice oxygen and metal ions in the $Pr_{0.3}BSCF$ nanocomposite. It may benefit oxygen ions' migration because it weakens the Coulombic force between B-site ions and O^{2-}, promoting the ORR performance.[24] We also found a higher binding energy of surface oxygen species, which were directly involved in ORR, for $Pr_{0.3}BSCF$ than BSCF (for example, 531.3 vs 531.0 eV for $-OH/O_2$), further inferring the more extraordinary ORR performance of the $Pr_{0.3}BSCF$ nanocomposite. In addition, with the Pr^{3+} occupying the A-site cation (Ba^{2+}, Sr^{2+}) lattice sites of BSCF, the oxygen anion will fill the oxygen vacancy due to electroneutrality, and the lattice oxygen content will increase accordingly. By estimating the molar fractions of various oxygen species from their respective relative areas, we can see an increased content of lattice oxygen for the $Pr_{0.3}BSCF$

https://doi.org/10.1021/acs.chemmater.4c02386
Chem. Mater. 2024, 36, 11288–11295

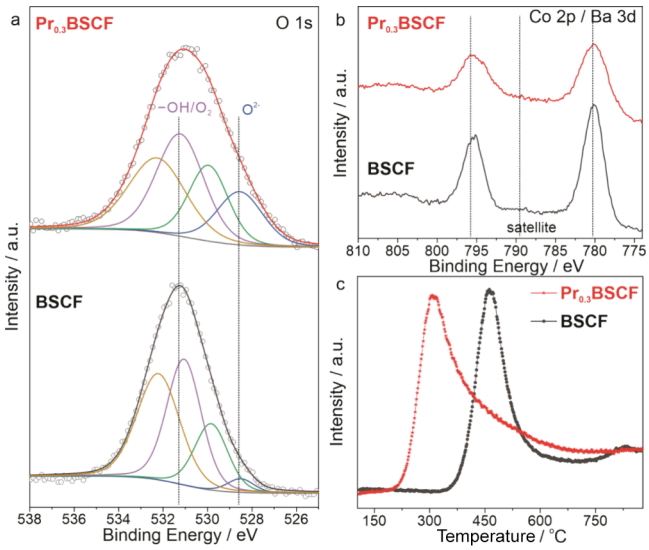

Figure 3. Intrinsic properties of the $Pr_{0.3}$BSCF nanocomposite. (a) O 1s and (b) Co 2p/Ba 3d core-level XPS results of the $Pr_{0.3}$BSCF nanocomposite and BSCF. (c) O_2-TPD for the $Pr_{0.3}$BSCF nanocomposite and BSCF from 120 to 880 °C.

nanocomposite (Table S2). Interestingly, compared with BSCF, the $Pr_{0.3}$BSCF nanocomposite still shows similar molar fractions of surface-adsorbed oxygen species O_2^{2-}/O^-, which can be assigned to the surface oxygen vacancies of perovskite oxides.[23,25] It should be caused by the formation of unique secondary nanoparticles in the $Pr_{0.3}$BSCF nanocomposite.

We further studied the electronic structures of Co and Fe by XPS. Figure 3b shows the Co 2p core-level XPS spectra. Due to the overlap between Ba 3d and Co 2p main peaks (≈795 and ≈780 eV), it is challenging to deconvolute the Co valences by peak fitting. Nevertheless, it is possible to probe the Co valence state from the Co 2p satellite peak.[26,27] The relatively flatter satellite spectral shape of the $Pr_{0.3}$BSCF nanocomposite may indicate the presence of Co^{4+}.[27,28] We found a negligible shift for Fe 2p XPS spectra (Figure S6). It infers that the Pr dopant mainly affects the Co state but is insignificant for the surface Fe state. Based on these results, we propose a probable mechanism for forming twin phases of the $Pr_{0.3}$BSCF nanocomposite. The Pr doping could induce lattice contraction in BSCF, resulting in locally distorted B-site Co octahedra and the formation of secondary orthorhombic nanoparticles.

To get more insight into the valence state change upon the formation of the twin-phase nanocomposite, an O_2-TPD experiment was conducted (Figure 3c). There are two oxygen desorption peaks: The one at low temperature (300−600 °C) is usually ascribed to a valence change from Co^{4+}/Fe^{4+} to Co^{3+}/Fe^{3+} and the oxygen species on the surface desorption. Another peak at high temperature (~800 °C) is associated with a further decrease of valence from Co^{3+}/Fe^{3+} to Co^{2+}/Fe^{2+} and lattice oxygen desorption.[29−31] Therefore, the process also sheds light on oxygen surface exchange and bulk diffusion. For the $Pr_{0.3}$BSCF nanocomposite, the desorption peak at the low-temperature zone shifted toward lower temperatures than the BSCF. It suggests improved O bulk diffusion and surface exchange.[29,30] We also found that the desorption peak for the $Pr_{0.3}$BSCF nanocomposite at the high-temperature zone from 750 to 880 °C was depressed, while a clear peak showed for BSCF. It indicates the improved structural stability of the $Pr_{0.3}$BSCF nanocomposite as less lattice oxygen is desorbed even at 880 °C.[29,30] In other words, the formation of the nanocomposite structure suppressed the reduction of Co^{3+} and Fe^{3+} but promoted the reduction of Co^{4+}/Fe^{4+} to Co^{3+}/Fe^{3+}. The results also indicate improved ORR performance and excellent stability during applications.

It is well-known that the biggest challenge of the application of BSCF in PCFCs is due to its structural instability at typical operation temperatures.[15,32] It will undergo a structural transition from the corner-shared cubic phase to the face-shared hexagonal phase at temperatures below 800 °C (Figure S7).[30,32,33] Such transitions would reduce the oxygen transport, weaken the connection between the electrolyte and cathode, and eventually lead to the deterioration of the fuel cells. Figure 4a shows additional peaks associated with the hexagonal phase

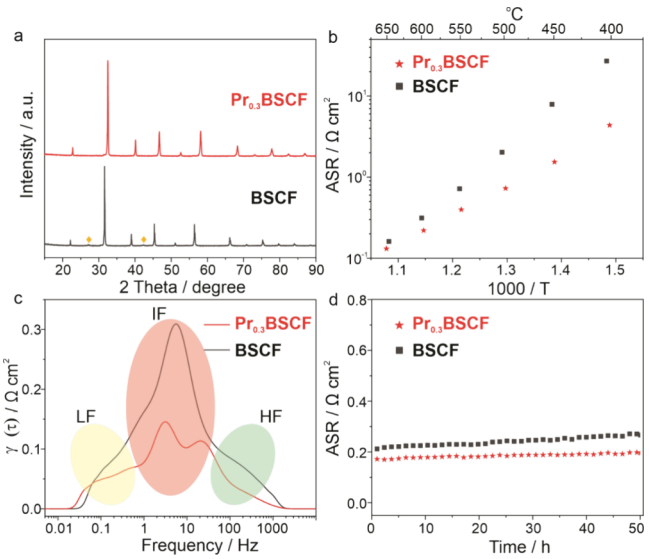

Figure 4. Thermal stability and symmetrical cell performances of the $Pr_{0.3}$BSCF nanocomposite. (a) XRD patterns of the $Pr_{0.3}$BSCF nanocomposite and BSCF powders after being calcined in humid air (3% H_2O) at 650 °C for 100 h. (b) Temperature-dependent polarization resistances of the $Pr_{0.3}$BSCF nanocomposite and BSCF cathode in wet air (3% H_2O) based on BCZYYb-supported symmetrical cells. (c) Corresponding DRT plots at 550 °C. (d) The long-term stability of the ASRs of the $Pr_{0.3}$BSCF nanocomposite and BSCF cathodes at 600 °C in wet air (3% H_2O) based on the symmetrical cells.

appearing after calcination of BSCF at 650 °C for 100 h. However, no additional XRD peaks were observed for the $Pr_{0.3}$BSCF nanocomposite (Figure S8). We further confirmed the structural stability of the $Pr_{0.3}$BSCF nanocomposite by Raman spectroscopy (Figure S9). The nanocomposite shows excellent thermal stability at low operation temperatures, paving the way for its application in PCFCs.

We first used EIS to evaluate the ORR activity of the $Pr_{0.3}$BSCF nanocomposite on BCZYYb-supported symmetric cells at varied temperatures (400−650 °C). As shown in Figure 4b, the $Pr_{0.3}$BSCF nanocomposite achieves area-specific resistance (ASR) values of 0.131, 0.220, 0.398, 0.728, 1.539, and 4.379 Ω cm^2 at 650, 600, 550, 500, 450, and 400 °C in wet air, respectively. Under the same experimental conditions, the BSCF has significantly larger ASR values than the $Pr_{0.3}$BSCF nanocomposite across all the tested temperatures. For instance, the polarization resistance (R_p) of BSCF is 0.720 Ω cm^2 at 550

https://doi.org/10.1021/acs.chemmater.4c02386
Chem. Mater. 2024, 36, 11288−11295

°C, which is about 1.8 times that of the $Pr_{0.3}$BSCF nanocomposite. It is noted that the ASR values of the $Pr_{0.3}$BSCF nanocomposite are lower than those of state-of-the-art nanocomposite cathodes for PCFCs, demonstrating the exceptional performance of the as-prepared nanocomposite electrodes (Table S3). Furthermore, the activation energy (E_a) of the $Pr_{0.3}$BSCF nanocomposite is only 71.84 kJ/mol, which is substantially smaller than that of reported nanocomposite electrodes and other promising benchmark triple-conducting cathode electrodes, including $BaCo_{0.4}Fe_{0.4}Zr_{0.1}Y_{0.1}O_{3-\delta}$ (88.77 kJ/mol),[1] $Ba_{0.875}Fe_{0.875}Zr_{0.125}O_{3-\delta}$ (95.90 kJ/mol),[32] $PrBa_{0.5}Sr_{0.5}Co_{2-x}Fe_xO_{5+\delta}$ (114.48 kJ/mol),[34] and $Gd_{0.3}Ca_{2.7}Co_{3.82}Cu_{0.18}O_{9-\delta}$ (81.05 kJ/mol).[35] The low E_a of the $Pr_{0.3}$BSCF nanocomposite suggests its great potential as a cathode candidate for PCFCs.

To further understand the role of the $Pr_{0.3}$BSCF nanocomposite in promoting the ORR, the EIS data were analyzed using the distribution of relaxation time (DRT) model.[36] The DRT method could reveal the kinetics of the catalytic ORR processes by deconvoluting complex electrochemical impedance spectra data.[4,37] As illustrated in Figure 4c, there are several separate peaks that can be classified into high-frequency (HF), intermediate-frequency (IF), and low-frequency (LF) ranges. It has been suggested that HF peaks stand for the resistance of charge transfer processes between the electrolyte and the cathode interface; the IF peaks represent the resistance from surface exchange and bulk ion diffusion processes, whereas the LF peaks belong to the resistance of gas diffusion within the electrodes.[37−39] The area of the peaks correlates with the resistance of the corresponding electrochemical processes. Compared with BSCF, the $Pr_{0.3}$BSCF nanocomposite shows a significant decrease in the whole range, especially in the IF and HF areas, implying boosted charge transfer at the triple-phase boundary and improved surface exchange and bulk diffusion processes during ORR.[37−39] These results are consistent with the above XPS and O_2-TPD analyses. The superior performance of the $Pr_{0.3}$BSCF nanocomposite could be attributed to the beneficial synergistic effects between cubic and orthorhombic phases. The Co-rich cubic phase facilitates the transport of oxygen vacancy and electron holes, and the secondary rhombohedral phase may expedite the transport of protonic carriers.[40−42] Meanwhile, the $Pr_{0.3}$BSCF nanocomposite exhibits an excellent operational stability. As shown in Figure 4d, its ASR values showed a negligible degradation rate of 0.00046 Ω cm^2 h^{-1} in wet air at 600 °C during the 50 h test. In contrast, BSCF showed continual degradation with a 0.00130 Ω cm^2 h^{-1} rate. Overall, these results imply the excellent performance of the $Pr_{0.3}$BSCF nanocomposite as a cathode electrode of PCFCs.

To assess the performance of the $Pr_{0.3}$BSCF nanocomposite for PCFCs, an anode-supported single cell with a configuration of Ni-BCZYYb|BCZYYb|$Pr_{0.3}$BSCF was manufactured (Figure S10). *I*−*V*−*P* curves of the single cells are presented in Figure 5a. The cell shows a PPD of 1.02, 0.75, 0.50, 0.30, and 0.17 W cm^{-2} at 600, 550, 500, 450, and 400 °C, respectively. The BSCF-based single cell exhibits a PPD of 0.45, 0.30, 0.20, 0.10, and 0.05 W cm^{-2} at 600, 550, 500, 450, and 400 °C, respectively (Figure S11). The values are consistent with the reported data.[43] The performance of the $Pr_{0.3}$BSCF nanocomposite is twofold that of BSCF. It stands out among the reported state-of-the-art cathode electrodes for PCFCs under similar configuration and test conditions (Table S4). The excellent performance of the $Pr_{0.3}$BSCF nanocomposite was

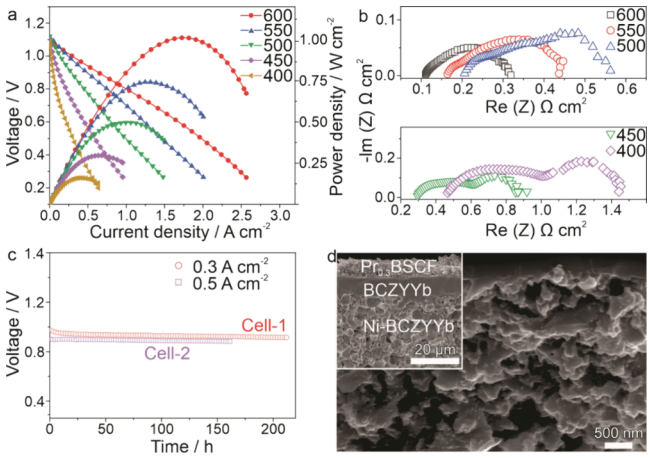

Figure 5. Electrochemical performance and stability of the $Pr_{0.3}$BSCF nanocomposite. (a) *I*−*V* and *I*−*P* curves of a Ni-BCZYYb|BCZYYb|$Pr_{0.3}$BSCF single cell at different temperatures. (b) Corresponding EIS spectra of the single cell at the OCV. (c) Long-term stability of the two single cells operated at constant current densities of 0.3 and 0.5 A cm^{-2} at 550 °C. (d) SEM image of the $Pr_{0.3}$BSCF nanocomposite after 0.3 A cm^{-2} for 210 h. Inset is the cross-sectional SEM image of the single cell after the stability test.

confirmed by its small polarizations measured by EIS (Figure 5b). The R_p values are 0.191, 0.279, 0.352, 0.571, and 0.998 Ω cm^2 at 600, 550, 500, 450, and 400 °C, respectively. Furthermore, the single cell with the $Pr_{0.3}$BSCF nanocomposite cathode electrode shows excellent operational stability of over ∼210 h at a current density of 0.3 A cm^{-2} with a degradation rate of 0.000271 V h^{-1} and over ∼160 h at a current density of 0.5 A cm^{-2} with a degradation rate of 0.000117 V h^{-1} at 550 °C (Figure 5c). After long-term stability testing, a robust microstructure of the single cell without delamination was preserved (Figure 5d). More importantly, the size of the secondary nanoparticles was maintained without detectable agglomeration. It can be attributed to the heterogeneous structures' "self-assembly" formation process during synthesis.[4,7,31,34,38] These findings confirm and demonstrate the unique structural advantages of the $Pr_{0.3}$BSCF nanocomposite as a promising cathode in PCFCs. The nanoscale contact between the twin phases could preserve large concentrations of active sites. Meanwhile, their strong interphase interaction could shorten the diffusion paths, accelerate the charge transfer of ions and electrons, limit thermal expansion and structural transformation, and collaboratively contribute to excellent activity and stability.[7,12]

■ CONCLUSIONS

In conclusion, this work reported successfully engineering a coupled $Pr_{0.3}$BSCF nanocomposite as a promising cathode electrode for PCFCs. The smaller Pr^{3+} cation dopant shrinks the crystal lattice of cubic BSCF. It causes the B-site cations to distort, forming a secondary orthorhombic structure, which is uniformly distributed and intimately contacted at the nanoscale on bulk particles. This new cathode showed great ORR activity and excellent operational stability. It achieved a high PPD of 1.02 W cm^{-2} at 600 °C and maintained excellent stability at a current density of 0.3 A cm^{-2} for 210 h at 550 °C. The $Pr_{0.3}$BSCF nanocomposite's performance exceeds most reported nanocomposite cathodes and state-of-the-art benchmark triple-conducting cathode electrodes. The outstanding

https://doi.org/10.1021/acs.chemmater.4c02386
Chem. Mater. 2024, 36, 11288−11295

performance of the $Pr_{0.3}$BSCF nanocomposite could be attributed to its unique structural advantages, such as a homogeneous component distribution with robust and infinite interfaces and synergistic effects. This study offers a promising avenue for advancing high-performance electrocatalysts for PCFCs and other applications.

■ ASSOCIATED CONTENT

Supporting Information

The Supporting Information is available free of charge at https://pubs.acs.org/doi/10.1021/acs.chemmater.4c02386.

EDS spectra, HAADF-STEM image and mapping, XPS of the $Pr_{0.3}$BSCF nanocomposite; SEM, HAADF-STEM images, mapping of the BSCF; stability analysis by XRD and Raman spectroscopy; photograph of the single cell; single cell performances for BSCF; tables for the atomic percentage and XPS peak deconvolution results of O 1s of the $Pr_{0.3}$BSCF nanocomposite; and tables for the ASR and PPD comparison (PDF)

■ AUTHOR INFORMATION

Corresponding Authors

Jiawei Zhang − *Department of Materials Science and Engineering, Clemson University, Clemson, South Carolina 29634, United States*; Email: bosszjw@gmail.com

Jianhua Tong − *Department of Materials Science and Engineering, Clemson University, Clemson, South Carolina 29634, United States*; orcid.org/0000-0002-0684-1658; Email: jianhut@clemson.edu

Authors

Liang Han − *Department of Materials Science and Engineering, Clemson University, Clemson, South Carolina 29634, United States*

Minda Zou − *Department of Materials Science and Engineering, Clemson University, Clemson, South Carolina 29634, United States*; orcid.org/0000-0001-9146-9581

Yuchen Zhang − *Department of Materials Science and Engineering, Clemson University, Clemson, South Carolina 29634, United States; Energy & Environmental Science and Technology, Idaho National Laboratory, Idaho Falls, Idaho 83401, United States*; orcid.org/0000-0001-5734-948X

Hongkui Zheng − *Department of Materials Science and Engineering, University of California, Irvine, California 92697, United States*

Ryo Kitamura − *Department of Materials Science and Engineering, Clemson University, Clemson, South Carolina 29634, United States*

Yanfei Cai − *Department of Materials Science and Engineering, Clemson University, Clemson, South Carolina 29634, United States*

Talia Marie Sebastian − *Ground Vehicle Systems Center (GVSC), Detroit Arsenal, Warren, Michigan 48397, United States*

Ted Burye − *Ground Vehicle Systems Center (GVSC), Detroit Arsenal, Warren, Michigan 48397, United States*

Dong Ding − *Energy & Environmental Science and Technology, Idaho National Laboratory, Idaho Falls, Idaho 83401, United States*; orcid.org/0000-0002-6921-4504

Zeyu Zhao − *Energy & Environmental Science and Technology, Idaho National Laboratory, Idaho Falls, Idaho 83401, United States*

Kai He − *Department of Materials Science and Engineering, University of California, Irvine, California 92697, United States*; orcid.org/0000-0003-4666-1800

Complete contact information is available at: https://pubs.acs.org/10.1021/acs.chemmater.4c02386

Notes

The authors declare no competing financial interest.

■ ACKNOWLEDGMENTS

This work was supported by Clemson University's Virtual Prototyping of Autonomy Enabled Ground Systems (VIPR-GS) under Cooperative Agreement W56HZV-21-2-0001 with the US Army DEVCOM Ground Vehicle Systems Center (GVSC). This work was also partially supported by the US Department of Energy's Office of Fossil Energy and Carbon Management (FECM) Award DE-FE0031871 and the National Aeronautics and Space Administration (NASA) under Grant 80NSSC20M0233 (NASA). H.Z. and K.H. acknowledge the support by the National Science Foundation (NSF) under Award Number 2239598, as well as the use of facilities and instrumentation at the University of California Irvine Materials Research Institute, supported in part by the National Science Foundation Materials Research Science and Engineering Center program through the University of California Irvine Center for Complex and Active Materials (DMR-2011967). Z. Z. and D. D. would like to thank funding supported by the proton conducting solid oxide electrolysis cells (P-SOEC) lab call project from the U.S. Department of Energy (USDOE); the Office of Energy Efficiency and Renewable Energy (EERE); the Hydrogen and Fuel Cell Technologies Office (HFTO) under DOE Idaho Operations Office under contract no. DE-AC07-05ID14517. The authors acknowledge Dimuthu Edirisinghe and Dr. George Chumanov (Department of Chemistry, Clemson University) for help with the Raman spectroscopy measurement. DISTRIBUTION STATEMENT A. Approved for public release: Distribution is Unlimited. OPSEC 8910

■ REFERENCES

(1) Duan, C.; Tong, J.; Shang, M.; Nikodemski, S.; Sanders, M.; Ricote, S.; Almansoori, A.; O'Hayre, R. Readily Processed Protonic Ceramic Fuel Cells with High Performance at Low Temperatures. *Science* **2015**, *349* (6254), 1321−1326.

(2) Huang, Y.; Qiu, R.; Lian, W.; Lei, L.; Liu, T.; Zhang, J.; Wang, Y.; Liu, J.; Huang, J.; Chen, F. Review: Measurement of Partial Electrical Conductivities and Transport Numbers of Mixed Ionic−electronic Conducting Oxides. *J. Power Sources* **2022**, *528*, No. 231201.

(3) Zhao, C.; Li, Y.; Zhang, W.; Zheng, Y.; Lou, X.; Yu, B.; Chen, J.; Chen, Y.; Liu, M.; Wang, J. Heterointerface Engineering for Enhancing the Electrochemical Performance of Solid Oxide Cells. *Energy Environ. Sci.* **2020**, *13* (1), 53−85.

(4) Niu, Y.; Zhou, Y.; Zhang, W.; Zhang, Y.; Evans, C.; Luo, Z.; Kane, N.; Ding, Y.; Chen, Y.; Guo, X.; Lv, W.; Liu, M. Highly Active and Durable Air Electrodes for Reversible Protonic Ceramic Electrochemical Cells Enabled by an Efficient Bifunctional Catalyst. *Adv. Energy Mater.* **2022**, *12* (12), No. 2103783.

(5) Chen, D.; Chen, C.; Baiyee, Z. M.; Shao, Z.; Ciucci, F. Nonstoichiometric Oxides as Low−cost and Highly−efficient Oxygen Reduction/Evolution Catalysts for Low−temperature Electrochemical Devices. *Chem. Rev.* **2015**, *115* (18), 9869−9921.

(6) Arandiyan, H.; Mofarah, S. S.; Sorrell, C. C.; Doustkhah, E.; Sajjadi, B.; Hao, D.; Wang, Y.; Sun, H.; Ni, B. J.; Rezaei, M.; Shao, Z.;

Maschmeyer, T. Defect Engineering of Oxide Perovskites for Catalysis and Energy Storage: Synthesis of Chemistry and Materials Science. *Chem. Soc. Rev.* **2021**, *50* (18), 10116−10211.
(7) Zhang, J.; Gao, M.; Luo, J. In Situ Exsolved Metal Nanoparticles: A Smart Approach for Optimization of Catalysts. *Chem. Mater.* **2020**, *32* (13), 5424−5441.
(8) Hu, T.; He, F.; Liu, M.; Chen, Y. In situ/operando Regulation of the Reaction Activities on Hetero−structured Electrodes for Solid Oxide Cells. *Prog. Mater. Sci.* **2023**, *133*, No. 101050.
(9) Yang, L.; Zuo, C.; Wang, S.; Cheng, Z.; Liu, M. A Novel Composite Cathode for Low−temperature SOFCs Based on Oxide Proton Conductors. *Adv. Mater.* **2008**, *20* (17), 3280−3283.
(10) Crumlin, E.; Mutoro, E.; Ahn, S.; La O', G.; Leonard, D.; Borisevich, A.; Biegalski, M.; Christen, H.; Shao-Horn, Y. Oxygen Reduction Kinetics Enhancement on a Heterostructured Oxide Surface for Solid Oxide Fuel Cells. *J. Phys. Chem. Lett.* **2010**, *1* (21), 3149−3155.
(11) Ding, D.; Li, X.; Lai, S. Y.; Gerdes, K.; Liu, M. Enhancing SOFC Cathode Performance by Surface Modification Through Infiltration. *Energy Environ. Sci.* **2014**, *7* (2), 552−575.
(12) Han, L.; Zhang, J.; Zou, M.; Tong, J. Toward Superb Perovskite Oxide Electrocatalysts: Engineering of Coupled Nanocomposites. *Small* **2022**, *18* (50), No. 2204784.
(13) Buzi, F.; Kreka, K.; Santiso, J.; Rapenne, L.; Sha, Z.; Douglas, J. O.; Chiabrera, F.; Morata, A.; Burriel, M.; Skinner, S.; Bernadet, L.; Baiutti, F.; Tarancon, A. A Self-Assembled Multiphasic Thin Film as an Oxygen Electrode for Enhanced Durability in Reversible Solid Oxide Cells. *ACS Appl. Mater. Interfaces* **2024**, *16* (33), 43462−43473.
(14) Ishii, A.; Nemoto, N.; Yamaguchi, M.; Kobayashi, K.; Oikawa, I.; Takano, A.; Hitomi, T.; Hayashi, N.; Takamura, H. Key Role of Interfacial Cobalt Segregation in Stable Low-Resistance Composite Oxygen-Reducing Electrodes. *ACS Appl. Mater. Interfaces* **2023**, *15* (29), 34809−34817.
(15) Xu, X.; Su, C.; Shao, Z. Fundamental Understanding and Application of $Ba_{0.5}Sr_{0.5}Co_{0.8}Fe_{0.2}O_{3-\delta}$ Perovskite in Energy Storage and Conversion: Past, Present, and Future. *Energy Fuels* **2021**, *35* (17), 13585−13609.
(16) Lim, D.; Singh, B.; Choi, M.; Song, S. Study of Hydration/Dehydration Kinetics of SOFC Cathode Material $Ba_{0.5}Sr_{0.5}Co_{0.8}Fe_{0.2}O_{3-\delta}$ by Electrical Conductivity Relaxation Technique. *J. Electrochem. Soc.* **2013**, *160* (8), F764−F768.
(17) Grimaud, A.; Mauvy, F.; Bassat, J.; Fourcade, S.; Rocheron, L.; Marrony, M.; Grenier, J. C. Hydration Properties and Rate Determining Steps of The Oxygen Reduction Reaction of Perovskite−related Oxides as H^+−SOFC Cathodes. *J. Electrochem. Soc.* **2012**, *159* (6), B683−B694.
(18) Jeon, S.; Lim, D.; Kim, I.; Singh, B.; Song, S. Effectiveness of Protonic Conduction in $Ba_{0.5}Sr_{0.5}Co_{0.8}Fe_{0.2}O_{3-\delta}$ Cathode in Intermediate Temperature Proton−conducting Ceramic−electrolyte Fuel Cell. *J. Electrochem. Soc.* **2014**, *161* (6), F754−F760.
(19) Efimov, K.; Xu, Q.; Feldhoff, A. Transmission Electron Microscopy Study of $Ba_{0.5}Sr_{0.5}Co_{0.8}Fe_{0.2}O_{3-\delta}$ Perovskite Decomposition at Intermediate Temperatures. *Chem. Mater.* **2010**, *22* (21), 5866−5875.
(20) Gomez, M. A.; Griffin, M. A.; Jindal, S.; Rule, K. D.; Cooper, V. R. The Effect of Octahedral Tilting on Proton Binding Sites and Transition States in Pseudo−cubic Perovskite Oxides. *J. Chem. Phys.* **2005**, *123* (9), No. 094703.
(21) Zhou, J.; Goodenough, J. B. Universal Octahedral−site Distortion in Orthorhombic Perovskite Oxides. *Phys. Rev. Lett.* **2005**, *94* (6), No. 065501.
(22) Zhu, Y.; Zhou, W.; Chen, Y.; Yu, J.; Liu, M.; Shao, Z. A High−performance Electrocatalyst for Oxygen Evolution Reaction: $LiCo_{0.8}Fe_{0.2}O_2$. *Adv. Mater.* **2015**, *27* (44), 7150−7155.
(23) Liu, R.; Liang, F.; Zhou, W.; Yang, Y.; Zhu, Z. Calcium−doped Lanthanum Nickelate Layered Perovskite and Nickel Oxide Nano−hybrid for Highly Efficient Water Oxidation. *Nano Energy* **2015**, *12*, 115−122.
(24) Zhang, Z.; Zhu, Y.; Zhong, Y.; Zhou, W.; Shao, Z. Anion Doping: A New Strategy for Developing High−performance Perovskite−type Cathode Materials of Solid Oxide Fuel Cells. *Adv. Energy Mater.* **2017**, *7* (17), No. 1700242.
(25) Li, G.; Hou, S.; Gui, L.; Feng, F.; Zhang, D.; He, B.; Zhao, L. Carbon Quantum Dots Decorated $Ba_{0.5}Sr_{0.5}Co_{0.8}Fe_{0.2}O_{3-\delta}$ Perovskite Nanofibers for Boosting Oxygen Evolution Reaction. *Appl. Catal. B: Environ.* **2019**, *257*, No. 117919.
(26) Zhu, Y.; Zhang, L.; Zhao, B.; Chen, H.; Liu, X.; Zhao, R.; Wang, X.; Liu, J.; Chen, Y.; Liu, M. Improving the Activity for Oxygen Evolution Reaction by Tailoring Oxygen Defects in Double Perovskite Oxides. *Adv. Funct. Mater.* **2019**, *29* (34), No. 1901783.
(27) Xu, X.; Chen, Y.; Zhou, W.; Zhu, Z.; Su, C.; Liu, M.; Shao, Z. A Perovskite Electrocatalyst for Efficient Hydrogen Evolution Reaction. *Adv. Mater.* **2016**, *28* (30), 6442−6448.
(28) Chen, G.; Zhou, W.; Guan, D.; Sunarso, J.; Zhu, Y.; Hu, X.; Zhang, W.; Shao, Z. Two Orders of Magnitude Enhancement in Oxygen Evolution Reactivity on Amorphous $Ba_{0.5}Sr_{0.5}Co_{0.8}Fe_{0.2}O_{3-\delta}$ Nanofilms with Tunable Oxidation State. *Sci. Adv.* **2017**, *3* (6), No. e1603206.
(29) Ge, L.; Zhou, W.; Ran, R.; Liu, S.; Shao, Z.; Jin, W.; Xu, N. Properties and Performance of A−site Deficient $(Ba_{0.5}Sr_{0.5})_{1-x}Co_{0.8}Fe_{0.2}O_{3-\delta}$ for Oxygen Permeating Membrane. *J. Membr. Sci.* **2007**, *306* (1−2), 318−328.
(30) Xie, Y.; Hu, X.; Shi, N.; Peng, R.; Chen, M.; Xia, C. La−doped $Ba_{0.5}Sr_{0.5}Co_{0.8}Fe_{0.2}O_{3-\delta}$ as Cathode for Protonic−conducting Solid Oxide Fuel Cells with Enhanced Structure Stability. *ECS Trans.* **2021**, *103* (1), 1525.
(31) Song, Y.; Chen, Y.; Wang, W.; Zhou, C.; Zhong, Y.; Yang, G.; Zhou, W.; Liu, M.; Shao, Z. Self−assembled Triple−conducting Nanocomposite as A Superior Protonic Ceramic Fuel Cell Cathode. *Joule* **2019**, *3* (11), 2842−2853.
(32) Niedrig, C.; Taufall, S.; Burriel, M.; Menesklou, W.; Wagner, S.; Baumann, S.; Ivers-Tiffée, E. Thermal Stability of The Cubic Phase in $Ba_{0.5}Sr_{0.5}Co_{0.8}Fe_{0.2}O_{3-\delta}$ (BSCF)1. *Solid State Ion.* **2011**, *197* (1), 25−31.
(33) Wang, Z.; Wang, Y.; Wang, J.; Song, Y.; Robson, M. J.; Seong, A.; Yang, M.; Zhang, Z.; Belotti, A.; Liu, J.; Kim, G.; Lim, J.; Shao, Z.; Ciucci, F. Rational Design of Perovskite Ferrites as High−performance Proton−conducting Fuel Cell Cathodes. *Nat. Catal.* **2022**, *5* (9), 777−787.
(34) Zhou, Y.; Zhang, W.; Kane, N.; Luo, Z.; Pei, K.; Sasaki, K.; Choi, Y.; Chen, Y.; Ding, D.; Liu, M. An Efficient Bifunctional Air Electrode for Reversible Protonic Ceramic Electrochemical Cells. *Adv. Funct. Mater.* **2021**, *31* (40), No. 2105386.
(35) Saqib, M.; Choi, I.; Bae, H.; Park, K.; Shin, J.; Kim, Y.; Lee, J.; Jo, M.; Kim, Y.; Lee, K.; Song, S.; Wachsman, E.; Park, J. Transition from Perovskite to Misfit−layered Structure Materials: A Highly Oxygen Deficient and Stable Oxygen Electrode Catalyst. *Energy Environ. Sci.* **2021**, *14* (4), 2472−2484.
(36) Li, H.; Lyu, Z.; Han, M. Robust and Fast Estimation of Equivalent Circuit Model from Noisy Electrochemical Impedance Spectra. *Electrochim. Acta* **2022**, *422*, No. 140474.
(37) Bello, I. T.; Song, Y.; Yu, N.; Li, Z.; Zhao, S.; Maradesa, A.; Liu, T.; Shao, Z.; Ni, M. Evaluation of The Electrocatalytic Performance of A Novel Nanocomposite Cathode Material for Ceramic Fuel Cells. *J. Power Sources* **2023**, *560*, No. 232722.
(38) Xia, J.; Zhu, F.; He, F.; Xu, K.; Choi, Y.; Chen, Y. Self−Configured Composites of Ruddlesden−Popper Perovskite and Pr_6O_{11} as Efficient and Durable Air Electrodes for Reversible Protonic Ceramic Electrochemical Cells. *Adv. Energy Mater.* **2023**, *13* (46), No. 2302964.
(39) Song, Y.; Liu, J.; Wang, Y.; Guan, D.; Seong, A.; Liang, M.; Robson, M. J.; Xiong, X.; Zhang, Z.; Kim, G.; Shao, Z.; Ciucci, F. Nanocomposites: A New Opportunity for Developing Highly Active and Durable Bifunctional Air Electrodes for Reversible Protonic Ceramic Cells. *Adv. Energy Mater.* **2021**, *11* (36), No. 2101899.
(40) Liu, Q.; Li, R.; Feng, W.; Li, J.; Zhang, X.; Lv, H.; Shen, Y.; Song, Y.; Wang, G.; Bao, X. Promoting High−temperature Oxygen

Evolution Reaction via Infiltration of $PrCoO_{3-\delta}$ Nanoparticles. *ACS Appl. Energy Mater.* **2022**, *5* (9), 11604−11612.
(41) Chen, Y.; Choi, Y.; Yoo, S.; Ding, Y.; Yan, R.; Pei, K.; Qu, C.; Zhang, L.; Chang, I.; Zhao, B.; Zhang, Y.; Chen, H.; Chen, Y.; Yang, C.; deGlee, B.; Murphy, R.; Liu, J.; Liu, M. A Highly Efficient Multi−phase Catalyst Dramatically Enhances the Rate of Oxygen Reduction. *Joule* **2018**, *2* (5), 938−949.
(42) Ding, H.; Wu, W.; Jiang, C.; Ding, Y.; Bian, W.; Hu, B.; Singh, P.; Orme, C. J.; Wang, L.; Zhang, Y.; Ding, D. Self−sustainable Protonic Ceramic Electrochemical Cells Using A Triple Conducting Electrode for Hydrogen and Power Production. *Nat. Commun.* **2020**, *11* (1), 1907.
(43) Wan, T.; Zhu, A.; Li, H.; Wang, C.; Guo, Y.; Shao, Z.; Savadogo, O. Performance Variability of $Ba_{0.5}Sr_{0.5}Co_{0.8}Fe_{0.2}O_{3-\delta}$ Cathode on Proton−conducting Electrolyte SOFCs with Ag and Au Current Collectors. *Rare Metals* **2018**, *37* (8), 633−641.

https://doi.org/10.1021/acs.chemmater.4c02386
Chem. Mater. 2024, 36, 11288−11295